Chemical Science

ROYAL SOCIETY OF CHEMISTRY

EDGE ARTICLE

View Article Online
View Journal | View Issue

Cite this: *Chem. Sci.*, 2024, **15**, 4095

All publication charges for this article have been paid for by the Royal Society of Chemistry

Received 15th December 2023
Accepted 1st February 2024

DOI: 10.1039/d3sc06753j

rsc.li/chemical-science

Catalytic reduction of oxygen to water by non-heme iron complexes: exploring the effect of the secondary coordination sphere proton exchanging site†

Aakash Santra, Avijit Das, Simarjeet Kaur, Priya Jain, Pravin P. Ingole and Sayantan Paria *

In this study, we prepared non-heme Fe^{III} complexes (**1**, **2**, and **3**) of an N_4 donor set of ligands (H_2L, Me_2L, and BPh_2L). **1** is supported by a monoanionic bispyridine-dioxime ligand (HL). In **2** and **3**, the primary coordination sphere of Fe remained similar to that in **1**, except that the oxime protons of the ligand were replaced with two methyl groups and a bridging $-BPh_2$ moiety, respectively. X-ray structures of the Fe^{II} complexes (**1a** and **3a**) revealed similar Fe–N distances; however, they were slightly elongated in **2a**. The Fe^{III}/Fe^{II} potential of **1**, **2**, and **3** appeared at −0.31 V, −0.25 V, and 0.07 V *vs.* Fc^+/Fc, respectively, implying that HL and Me_2L have comparable donor properties. However, BPh_2L is more electron deficient than HL or Me_2L. **1** showed electrocatalytic oxygen reduction reaction (ORR) activity in acetonitrile in the presence of trifluoroacetic acid (TFAH) as the proton source at $E_{cat/2} = -0.45$ V and revealed selective $4e^-/4H^+$ reduction of O_2 to H_2O. **1** showed an effective overpotential (η_{eff}) of 0.98 V and turnover frequency (TOF_{max}) of 1.02×10^3 s^{-1}. Kinetic studies revealed a k_{cat} of 2.7×10^7 M^{-2} s^{-1}. Strikingly, **2** and **3** remained inactive for electrocatalytic ORR, which established the essential role of the oxime scaffolds in the electrocatalytic ORR of **1**. Furthermore, a chemical ORR of **1** has been investigated using decamethylferrocene as the electron source. For **1**, a similar rate equation was noted to that of the electrocatalytic pathway. A k_{cat} of 6.07×10^4 M^{-2} s^{-1} was found chemically. Complex **2**, however, underwent a very slow chemical ORR. Complex **3** chemically enhances the $4e^-/4H^+$ reduction of O_2 and exhibits a TOF of 0.24 s^{-1} and a k_{cat} value of 2.47×10^2 M^{-1} s^{-1}. Based on the experimental observations, we demonstrate that the oxime backbone of the ligand in **1** works as a proton exchanging site in the $4e^-/4H^+$ reduction of O_2. The study describes how the ORR is affected by the tuning of the ligand scaffold in a family of non-heme Fe complexes.

Introduction

Cytochrome c oxidase (CcO), a terminal oxidase of the respiratory enzymes, is present in the mitochondrial membrane of all eukaryotes and many aerobic bacteria, and is responsible for the four-electron ($4e^-$)/four-proton ($4H^+$) reduction of oxygen (O_2) to water (H_2O) and protons.[1] The exergonic reaction is a reverse process of photosystem II, which is coupled with proton pumping, and the generated chemiosmotic potential in the process is used for ATP synthesis. Multicopper oxidases also perform the oxygen reduction reaction (ORR) to yield H_2O.[2,3] The development of efficient earth-abundant catalysts for the ORR is crucial, considering its importance in fuel cell technology and metal–air batteries.[4] Although Pt and PtM (M = Co, Ni, Cu, *etc.*) alloys are the most efficient catalysts for the ORR,[5] the less natural abundance and high cost of Pt considerably preclude its widespread application.

The ORR catalyzed by molecular complexes is particularly interesting because of the clear understanding of the active-site structure, reaction mechanism, and easy tuning of electronic properties around the metal center.[6–8] Different coordination complexes of 3d transition metal ions have been explored for electrocatalytic ORR.[6–9] Major efforts were made to develop molecular catalysts of different macrocyclic ligands, such as porphyrin, corrole, and phthalocyanine derivatives.[6–9] However, a limited number of non-heme complexes are known as ORR catalysts.[10–12] Iron is one of the most frequently found metal ions at the active site of versatile nonheme enzymes involved in a variety of small molecule transformation reactions.[13,14] The activation of dioxygen at the reduced Fe^{II} center and subsequent oxygenation of different substrates are known in versatile non-

Department of Chemistry, Indian Institute of Technology Delhi, Hauz Khas, New Delhi 110016, India. E-mail: sparia@chemistry.iitd.ac.in

† Electronic supplementary information (ESI) available. CCDC 2290392, 2290393 and 2314421. For ESI and crystallographic data in CIF or other electronic format see DOI: https://doi.org/10.1039/d3sc06753j

heme Fe enzymes such as α-keto glutarate dependent oxygenase, catechol dioxygenases, lipoxygenases, pterin-dependent hydroxylases, rieske dioxygenases, *etc.*[13,14] Additionally, a variety of oxygen-bound Fe intermediates have been characterized in the non-heme iron enzymes using small molecule model complexes.[15–17] However, examples of molecular nonheme Fe complexes for ORR studies are exceedingly rare.[18–23]

Nonheme Fe-based molecular homogeneous catalysts reported for ORR studies are depicted in Chart 1. Duboc and coworkers described ORR studies using a dinuclear Fe^{II} thiolate-based catalyst. The complex was shown to catalyze the $2e^-/2H^+$ reduction of O_2 to H_2O_2 (~95%) in the presence of chemical reductants and $4e^-/4H^+$ reduction to H_2O (less than ~10% H_2O_2) under electrochemical reaction conditions.[19] Nam and coworkers reported the selective conversion of O_2 to H_2O using an Fe^{III} complex of a Tetra-Amido-Macrocyclic-Ligand (TAML) *via* the formation of a $[(TAML)Fe^{V}(O)]^-$ reaction intermediate.[23] Electrocatalytic ORR using an Fe^{III} complex of an N_3O donor set of ligand was described by Machan and coworkers. The catalyst revealed the selective conversion of O_2 to H_2O *via* the formation of H_2O_2 as an intermediate reaction product (2 + 2 reaction pathway).[21] Likewise, another nonheme Fe complex of a terpyridine-derived N_3O donor set of ligand catalyzed the chemical reduction of O_2 to H_2O following a 2 + 2 reaction pathway.[22] Other than the mentioned complexes, no other nonheme Fe complexes are known as ORR catalysts.

A cross-linked tyrosine residue present around the active site of CcO is thought to play an important role in cleaving the O–O bond of the Fe^{III}–O–O–Cu^{II} intermediate.[24] Inspired by CcO, the effect of secondary coordination sphere interactions in the biomimetic ORR catalysts, such as the presence of a proton relay site,[25–34] positively charged functional groups to exert an electrostatic effect around the redox-active metal ion,[35,36] functional groups which can facilitate hydrogen atom transfer (HAT) and proton-coupled electron transfer (PCET) reactions,[31,37] *etc.*, have been explored to understand the O–O bond cleavage mechanism in different M–porphyrin/corrole complexes. It was established that the presence of such secondary effects could control the key factors of the ORR, such as the reaction rate, overpotential, and product selectivity. However, nonheme complexes describing the effect of secondary coordination sphere interactions on the ORR are scarce[38–41] and, to date, are not known with any nonheme Fe complex.

Herein, we report the synthesis and characterization of an Fe^{III} complex (**1**) of a bis-pyridine-dioxime ligand (H_2L). To establish the importance of oxime protons in ORR, another Fe^{III} complex (**2**) was prepared where the oxime protons of H_2L are replaced with methyl groups (Me_2L). Additionally, an Fe^{III} complex (**3**) was prepared where the oxime oxygen atoms of H_2L are connected to a $-BPh_2$ group, which creates a macrocyclic ring around Fe (Scheme 1). The electrocatalytic and chemical ORR of **1** has been investigated in oxygen-saturated acetonitrile solution using trifluoroacetic acid (TFAH) as the source of protons. **1** was found to enhance electrocatalytic $4e^-/4H^+$ reduction of O_2. Strikingly, no ORR was observed electrocatalytically in the presence of **2** and **3**, establishing an important role of oxime protons towards the electrocatalytic ORR of **1**. A turnover frequency (TOF_{max}) of 1.02×10^3 s^{-1} and an overpotential of 0.98 V were observed for **1**. For the chemical ORR, decamethylferrocene (Fc*) was used as the reductant. **1** was found to enhance ORR chemically and revealed $4e^-/4H^+$ selectivity and a k_{cat} value of 6.07×10^4 M^{-2} s^{-1}. In contrast, the use of **2** resulted in a very slow chemical ORR. Complex **3**, however, revealed a chemical ORR and showed $4e^-/4H^+$ selectivity, exhibiting a different rate equation from that of **1**. Based on the experimental findings, the catalytic ORR mechanism of the Fe complexes has been discussed. We suggest that the ligand oxime backbone in **1** works as a proton-exchanging site in the catalytic cycle. The study represents the first example of the effect of a secondary coordination sphere proton exchanging site on the ORR study by a molecular non-heme Fe complex.

Results and discussion

Synthesis and characterization of iron complexes

Here, we utilized a bispyridine-dioxime ligand system (H_2L) for the preparation of Fe complexes. Furthermore, we designed and synthesized a methylated ligand (Me_2L), where the oxime protons of H_2L are replaced by the $-CH_3$ groups. The preparation and characterization of Me_2L are described in the ESI (Fig. S1–S4†).

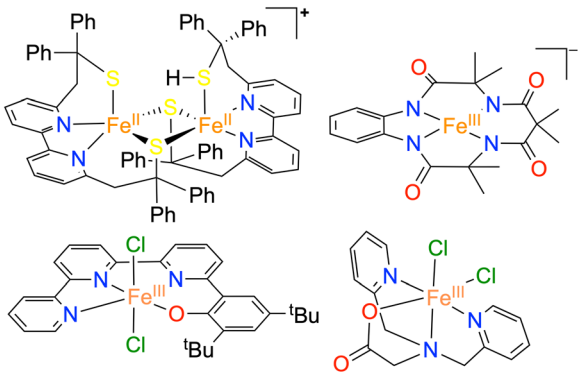

Chart 1 Structural depiction of the reported non-heme iron-based ORR catalysts.

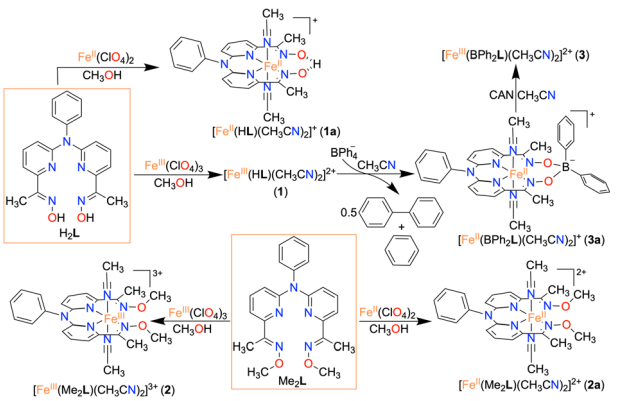

Scheme 1 Synthesis of the Fe complexes described in this study.

Fe^{III} (**1** and **2**) and Fe^{II} (**1a** and **2a**) complexes were prepared by mixing equimolar amounts of the ligand (H_2L or Me_2L) and $Fe^{III}(ClO_4)_3\cdot 6H_2O$ or $Fe^{II}(ClO_4)_2\cdot 6H_2O$ in methanol at 25 °C, respectively (Scheme 1). The Fe^{III} complexes are prepared under aerobic conditions. However, Fe^{II} complexes were synthesized inside an N_2-filled glove box. The ESI-mass spectrum of **1** revealed a molecular ion peak at $m/z = 416.08$ (Fig. S5†), which corresponds to the deprotonated ligand-coordinated Fe complex. The ^{1}H-NMR spectrum of **1** and **2** in CD_3CN revealed broad ligand proton resonances (Fig. S6 and S12†), suggesting the paramagnetic nature of the Fe^{III} complexes. Furthermore, we examined X-band EPR data of **1** in 9 : 1 methanol/ethanol at 77 K, which showed g values of 2.2, 2.17, and 1.96, confirming the presence of low-spin Fe^{III} in **1** (Fig. 1A). However, a g value of 4.22 was obtained in the EPR spectrum of **2**, implying the presence of high-spin Fe^{III} in **2**. The EPR data suggest that the methylation of the bispyridine-dioxime ligand causes the change of the Fe^{III} spin-state from $S = 1/2$ to 5/2. UV-vis spectrum of the Fe^{III} complexes in CH_3CN (Fig. 1B) revealed a charge-transfer transition at 468 nm ($\varepsilon = 1.27 \times 10^3\ M^{-1}\ cm^{-1}$) and 488 nm ($\varepsilon = 1.27 \times 10^3\ M^{-1}\ cm^{-1}$) for **1** and **2**, respectively. Furthermore, both the complexes exhibited ligand-derived $\pi \rightarrow \pi^*$ transitions at higher energy (below 360 nm).

The Fe^{II} complexes (**1a** and **2a**) were also thoroughly characterized by different spectroscopic techniques. Similar to **1**, **1a** revealed a molecular ion peak at $m/z = 416.08$ (Fig. S9†). The solid-state structure of **1a** is shown in Fig. 2A, where Fe is coordinated to the two imine and two pyridine nitrogen atoms ($d_{Fe-N(imine)} = 1.9041(18)$ and 1.8924(16) Å; $d_{Fe-N(pyridine)} = 1.9107$ (17) and 1.9019(16) Å) of the ligand at the equatorial plane, and axial positions are occupied by the acetonitrile molecules ($d_{Fe-N(CH_3CN)} = 1.9350(17)$ and 1.9275(16) Å). The X-ray structure of **2a** is shown in Fig. 2B. The Fe–$N_{pyridine}$ (1.933(3) and 1.930(2) Å) and Fe–N_{imine} (1.939(3) and 1.943(3) Å) distances in **2a** are slightly longer than the Fe–ligand bond distances observed in **1a**. The ligand O–O distance in **2a** is found to be 3.042 Å, which is considerably longer than the distance observed in **1a** (2.492 Å), implying that the intramolecular hydrogen bonding in **1a** makes the ligand cavity smaller.

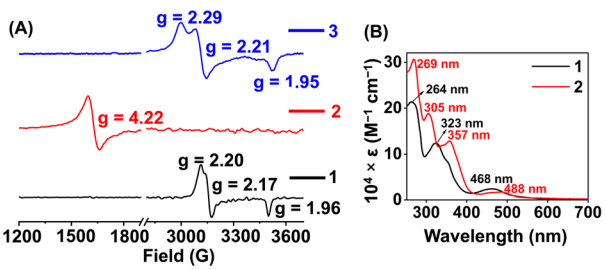

Fig. 1 (A) X-band EPR spectra of **1** (5 mM) and **2** (5 mM) in frozen 9 : 1 methanol/ethanol at 77 K. The EPR data of **3** (3 mM) were recorded in tetrahydrofuran at 77 K. $\nu = 9.631$ GHz, power = 2.71 mW, modulation frequency = 100 kHz, modulation amplitude = 4.91 G. (B) UV-vis spectra of **1** (0.5 mM) and **2** (0.5 mM) in acetonitrile at 25 °C.

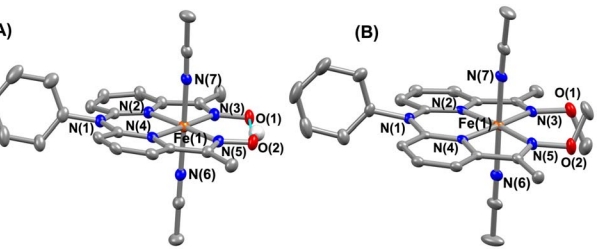

Fig. 2 X-ray structure of **1a** (A) and **2a** (B) with 50% ellipsoid probability. All hydrogen atoms except those attached to the oxime moiety have been omitted for clarity.

The ^{1}H-NMR spectra of the Fe^{II} complexes (in CD_3CN) are described in Fig. 3C, revealing sharp signals for the ligand proton resonance. The acidic OH proton of the ligand scaffold in **1a** appeared at 20 ppm. The methyl protons of the ligand (–(CH_3)C=N–O) were observed at 2.82 ppm and 3.42 ppm in **1a**. In **2a**, both methyl protons are observed at 3.03 ppm and the –OCH_3 protons at 4.00 ppm. Then, we examined the Fe^{II} complexes by UV-vis spectroscopy in acetonitrile (Fig. 3A). **1a** revealed a strong absorption band at 481 nm, which can be assigned to metal-to-ligand charge-transfer (MLCT).[42] In **2a**, the MLCT bands are observed at 486 nm. Additionally, ligand-based $\pi \rightarrow \pi^*$ transition at around 340 nm was observed in all of the Fe complexes.[41,43]

Interestingly, when we conducted the reaction of **1** with an excess of sodium tetraphenylborate in acetonitrile at 25 °C, the formation of a borylated Fe^{II} complex (**3a**) occurred, where the oxygen atoms of the ligand attached to the $-BPh_2$ moiety and created a six-membered ring around Fe (Scheme 1). Analysis of the reaction solution by GC-mass revealed the formation of biphenyl and benzene as the BPh_4^- derived product (Fig. S19†).

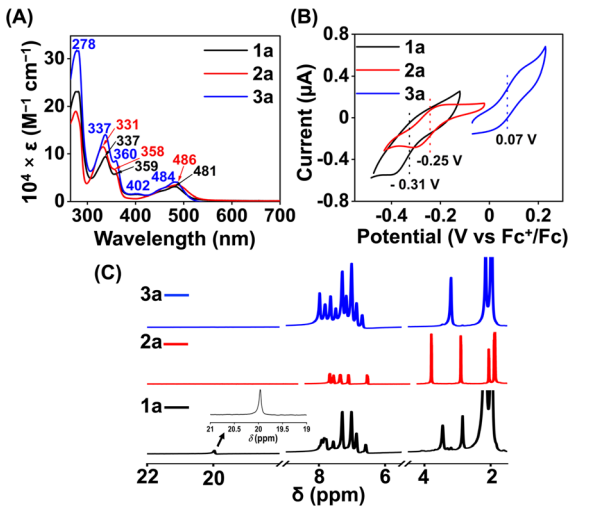

Fig. 3 (A) UV-vis spectra of **1a** (0.5 mM), **2a** (0.5 mM), and **3a** (0.5 mM) in acetonitrile at 25 °C. (B) Cyclic voltammogram of the Fe^{II} complexes (0.5 mM) in acetonitrile containing 50 mM of $^nBu_4NPF_6$ as the supporting electrolyte at 25 °C (scan rate 5 mV s^{-1}), using a 3 mm glassy carbon working electrode and Pt wire counter electrode. (C) ^{1}H-NMR spectrum of the Fe^{II} complexes in CD_3CN at 25 °C.

A proposed mechanism for the formation of **3a** from **1** has been described in Scheme S2.† The borylated ligand system has been defined as BPh_2**L** throughout the manuscript. The Fe^{II} complex (**3a**) was characterized thoroughly by different spectroscopic techniques. The ESI-mass spectrum of **3a** revealed a molecular ion peak at m/z = 580.16 (Fig. S18†), corresponding to a composition of $[(BPh_2L)Fe]^+$. The X-ray structure of **3a** is described in Fig. 4. Like **1a**, a similar coordination geometry around Fe was observed in **3a**, and the $d_{Fe-N(imine)}$ (1.882(2) and 1.882(2) Å), $d_{Fe-N(pyridine)}$ distances (1.906(2) and 1.901(2) Å) were found comparable to that of **1a**. The observed Fe–N_{imine} bond distances of **3a** are also comparable to the Fe–N_{imine} bond lengths reported in the borylated (dioximato)Fe^{II} complexes.[44] In addition, the Fe–N_{CH_3CN} distances of **3a** ($d_{Fe-N(CH_3CN)}$ = 1.950(2) and 1.932(2) Å) are also similar to **1a**. The boron atom of the –BPh_2 arm in **3a** sits 0.497 Å above the plane connecting four donor nitrogen atoms of the ligand. Furthermore, the N(3)–Fe(1)–N(5) angle observed in **3a** (97.92(10)°) is also comparable to **1a** (97.78(7) °), implying that the structural parameters of **3a** are not altered considerably compared to **1a** because of the borylated ring formation in **3a**. However, one of the axially coordinated acetonitrile molecules in **3a** is slightly bent (∠Fe(1)–N(6)–C(21) = 173.67°) compared to the other axial CH_3CN (176.28°), and the axially coordinated CH_3CN molecules in **1a**, which we suggest is because the phenyl ring of the –BPh_2 group remained nearly perpendicular to the plane of the donor nitrogen atoms of the ligand in **3a.**

The electronic spectrum of **3a** in acetonitrile is comparable to that of **1a** or **2a**, as described in Fig. 3A. The ^{1}H NMR spectrum of **3a** (Fig. 3C) exhibited features similar to that of **1a** or **2a**. The methyl protons of the ligand were observed at 3.17 ppm in **3a**.

Furthermore, we recorded the X-band EPR spectrum of the Fe^{III} complex (**3**) of the BPh_2**L** ligand (Fig. 1A), which revealed a rhombic spectrum having g values of 2.29, 2.21, and 1.95. Thus, **3** is also a low-spin complex like **1**. The presence of a macrocyclic ring created by the ligand around Fe causes better interactions between Fe and ligand orbitals, likely responsible for the presence of low-spin Fe^{III} in **1** and **3**.

Cyclic voltammetry (CV) and differential pulse voltammetry (DPV) experiments of the Fe complexes were examined in acetonitrile containing an excess amount of ^{n}Bu_4NPF_6 as the supporting electrolyte. **1a** revealed Fe^{III}/Fe^{II} potential at –0.31 V *vs.* Fc^+/Fc redox couple (Fig. 3B). The value is more than 300 mV anodically shifted than the Fe^{III}/Fe^{II} potential of Fe(TPP),[34] implying that HL is more electron deficient than the tetraphenyl porphyrin (TPP) system. However, the E_{ox} value of **1a** in acetonitrile is comparable to the large family of biomimetic Fe–porphyrin complexes containing different functional groups at the secondary coordination sphere.[45] In **2a**, the Fe^{III}/Fe^{II} peak was observed at −0.25 V *vs.* Fc^+/Fc, which is slightly anodically shifted compred to **1a**, suggesting that both Me_2**L** and H_2**L** have similar ligand donor properties. However, in **3a**, the Fe^{III}/Fe^{II} redox couple shifted anodically at 0.07 V *vs.* Fc^+/Fc (Fig. 3B), implying that the installation of the –BPh_2 group caused the ligand system to be more electron deficient. Furthermore, **1** and **2** exhibited redox waves at −0.54 V and −1.0 V *vs.* Fc^+/Fc, respectively, which can be tentatively assigned as the Fe^{II}/Fe^{I} couple (Fig. S26†).

Electrocatalytic ORR

We examined the electrocatalytic ORR of the Fe complexes in an O_2-saturated acetonitrile solution in the presence of TFAH as the proton source. In the presence of an excess of TFAH (20 equiv.), the Fe^{III}/Fe^{II} potential of **1** is anodically shifted from −0.31 V to −0.25 V (Fig. 5A). In addition, a similar shift is noticed when CV data of **1a** were recorded in the presence of 20 equiv. of TFAH (Fig. S27†). However, in the presence of TFAH, no significant change in the ligand-based π → π* transition was observed at 337 nm in the UV-vis spectrum (Fig. S28†). To further gain insight into the protonation event, we measured the ^{1}H-NMR data of **1a** in the presence of an excess amount of TFAH in DMSO-d_6 (Fig. S30†). The hydrogen-bonded oxime proton, which was observed at 19.5 ppm, shifted to 11.4 ppm in the presence of an excess of TFAH, demonstrating that both oxime oxygens are protonated in the presence of an excess TFAH. The breakdown of the strong intramolecular hydrogen bonding causes a prominent upfield shift of the oxime protons in the ^{1}H-NMR data. Furthermore, the ^{1}H-NMR spectrum of a Zn^{II}Cl complex supported by H_2**L** was recorded in DMSO-d_6, which also showed oxime protons at around 11.4 ppm (Fig. S30†). The X-ray structure of the Zn^{II}Cl complex showed

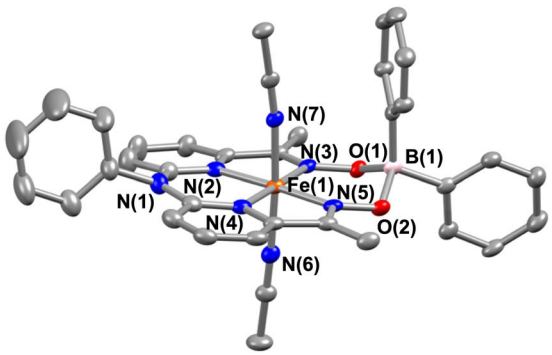

Fig. 4 X-ray structure of **3a** with 50% ellipsoid probability. All hydrogen atoms have been omitted for clarity.

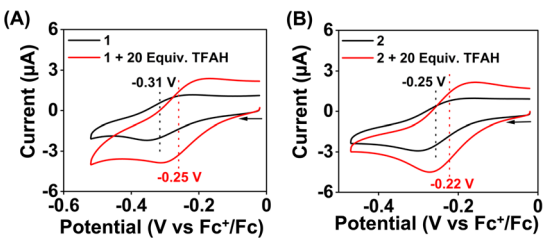

Fig. 5 Cyclic voltammogram of **1** (0.5 mM) (A) and **2** (0.5 mM) (B) in the presence and absence of excess TFAH (10 mM) in acetonitrile containing ^{n}Bu_4NPF_6 (50 mM) as the supporting electrolyte under a N_2 atmosphere (scan rate 0.1 V s^{-1}). A 3 mm glassy carbon working electrode and Pt wire counter electrode were used during the measurements.

that both of the oxime oxygen atoms are protonated.[41] Thus, we infer that the slight anodic shift of the Fe^{III}/Fe^{II} redox potential is because of the protonation of the oxime backbone of **1a**, which makes the ligand more electron-deficient. It's important to note here that the protonation of the oxime backbone of Co diimine–dioxime complexes has caused the shift of the electrocatalytic hydrogen evolution peak anodically in the presence of added acid.[46] However, the observed anodic shift for **1**/**1a** is not very large compared to the protonation event reported for the iron–porphyrin complexes containing secondary coordination sphere amine groups.[34] For example, an Fe^{III} porphyrin complex having *tert*-amine groups present at the secondary coordination sphere showed a 200 mV anodic shift of Fe^{III}/Fe^{II} potential in the presence of *p*-toluenesulfonic acid.[34] Furthermore, it's important to note here that a slight anodic shift of the Fe^{III}/Fe^{II} potential of **2**/**2a** was also noted (−0.22 V *vs.* Fc^{+}/Fc couple) in the presence of an excess TFAH (Fig. 5B and S31†), which we infer as the formation of the hydrogen-bonded adduct, as described in Chart S1.† The addition of TFAH to the acetonitrile solution of **3a** resulted in a cathodic shift of Fe^{III}/Fe^{II} potential to −0.25 V *vs.* Fc^{+}/Fc (Fig. S32†), which implies the coordination of TFAH to the Fe center responsible for the cathodic shift. Thus, the Fe^{III}/Fe^{II} potential of the Fe complexes of the three ligand systems (H_2L, Me_2L, and BPh_2L) discussed here in the presence of TFAH showed comparable potential values (−0.25 V, −0.22 V, and −0.25 V *vs.* Fc^{+}/Fc, respectively).

Upon cathodic scan, an irreversible current was observed in an O_2 saturated reaction solution of **1** (Fig. S33†), suggesting coordination of O_2 to the Fe^{II} center. In the presence of O_2 and TFAH, **1** exhibited a catalytic current at the position of the Fe^{III}/Fe^{II} redox couple ($E_{cat/2} = -0.45$ V *vs.* Fc^{+}/Fc couple, Fig. 6A), and no current enhancement was observed in the absence of O_2 (Fig. 6A), confirming the occurrence of catalytic ORR. A rinse test experiment confirms that the electrode-adsorbed material is not responsible for the observed catalytic current (Fig. S34†). The product selectivity for the ORR was evaluated by hydrodynamic voltammetry using an RRDE setup consisting of a glassy carbon disc and Pt ring electrode (Fig. S35†), which showed that **1** shows good selectivity for the $4e^{-}/4H^{+}$ reduction of O_2. While doing this measurement, it's assumed that transport-limited oxidation of H_2O_2 would occur in the Pt ring if formed in the ORR. However, a recent study revealed that the H_2O_2 oxidation at the Pt ring electrode is not transport-limited under the condition mostly employed in the nonaqueous RRDE analysis and could produce lower H_2O_2 yield if formed during the ORR.[47] Nevertheless, in this study, the absence of Pt ring current discards the possibility of the formation of H_2O_2 as an intermediate reaction product in the ORR of **1**.

In acetonitrile, **1** revealed an effective overpotential (η_{eff}) of 0.98 V (at $E_{cat/2} = -0.45$ V). The η_{eff} of **1** is comparable to the Fe–porphyrin catalysts for the ORR.[45]

Then, we examined the kinetics of electrocatalytic ORR in the presence of varying concentrations of the substrates. The pseudo-first-order rate constants (k_{obs}) were evaluated using eq (1).[48,49] Here, n_{cat} (=4) and n_p (=1) are the numbers of electrons associated with the catalytic process and Fe^{III}/Fe^{II} couple. *R*, *T*,

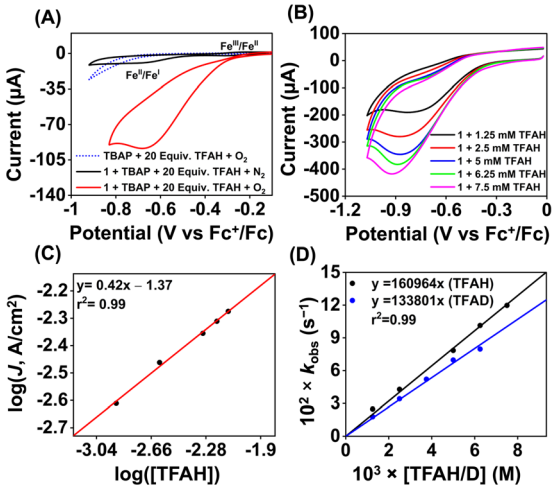

Fig. 6 (A) The cyclic voltammogram of **1** (0.5 mM) was measured in an oxygen-saturated acetonitrile solution containing 10 mM of TFAH and 50 mM $^{n}Bu_4NPF_6$ as the supporting electrolyte at 25 °C (scan rate 0.1 V s^{-1}). The black trace was taken in the absence of oxygen. The dotted blue trace was taken in the absence of **1** under oxygen. (B) Cyclic voltammogram of **1** (0.5 mM) measured at different concentrations of TFAH (1.25–7.5 mM) in oxygen-saturated acetonitrile with a scan rate of 6 V s^{-1} at 25 °C. (C) A plot of log(*J*, A cm^{-2}) *vs.* log([TFAH]) for **1** (0.5 mM) in oxygen saturated acetonitrile containing 50 mM $^{n}Bu_4NPF_6$ (scan rate 6 V s^{-1}). (D) A plot of k_{obs} *vs.* [TFAH/D] at a fixed concentration of **1** (0.5 mM) and O_2 (6.0 mM) at 25 °C.

and *F* are the Universal gas constant, temperature, and Faraday's constant, respectively. ν is the scan rate.

$$\frac{i_{cat}}{i_p} = \frac{n_{cat}}{0{\cdot}4463 n_p^{3/2}} \sqrt{\frac{RTk_{obs}}{F\nu}} \quad (1)$$

Initially, CV data of **1** (0.5 mM) were recorded in an oxygen-saturated acetonitrile solution containing 10 mM of TFAH at a variable scan rate (Fig. S36†), which revealed no increase of catalytic current above a scan rate of 6 V s^{-1}. Thus, we performed the substrate variation experiments at a scan rate of 6 V s^{-1}, where the pseudo-first-order reaction conditions are maintained in the diffusion layer.[50] The catalytic current was found to increase with an increasing concentration of the complex at a constant concentration of TFAH (10 mM) in oxygen-saturated acetonitrile (Fig. S37†). A plot of log(*J*, A cm^{-2}) *vs.* log([**1**]) follows a linear relationship, indicating first-order dependence (Fig. S38†). Likewise, at a constant concentration of **1** (0.5 mM), the catalytic current was found to increase with an increasing concentration of TFAH (ν = 6 V s^{-1}) (Fig. 6B). A plot of log(*J*, A cm^{-2}) *vs.* log([TFAH]) also follows a linear relationship (Fig. 6C), inferring first-order dependence. The k_{obs} values at different TFAH concentrations were extracted from the i_{cat} (under O_2) and i_p value (under N_2) using eqn (1). A k_{H^+} of 1.60 × 10^5 M^{-1} s^{-1} was obtained from the slope of a plot of k_{obs} *vs.* [TFAH] (Fig. 6D). Finally, the catalytic current was found to increase with increasing concentrations of O_2 at a fixed concentration of **1** (0.5 mM) and TFAH (10 mM), and first-order dependence was established (Fig. S39†). Thus, the rate equation for electrocatalytic ORR follows eqn (2) and (3).

$$\text{Rate} = k_{obs}[\mathbf{1}] \quad (2)$$

$$k_{obs} = k_{cat}[O_2]^1[TFAH]^1 \quad (3)$$

A k_{cat} of 2.7×10^7 M^{-2} s^{-1} was estimated using eqn (3), and from the slope of Fig. 6D. At a 10 mM TFAH concentration and scan rate of 6 V s^{-1}, a TOF of 1.02×10^3 s^{-1} has been estimated for **1**. Furthermore, we examined electrocatalytic ORR of **1** in the presence of trifluoroacetic acid-*d* (TFAD), which resulted in a k_{cat} of 2.25×10^7 M^{-2} s^{-1} and yielded a kinetic isotope effect (KIE = k^H_{cat}/k^D_{cat}) of 1.2 (Fig. 6D and S40†). The KIE value is rather small, suggesting the involvement of a proton-coupled electron transfer (PCET) reaction in the electrocatalytic ORR of **1**. For the PCET reaction, observation of a small KIE is known in different systems.[51]

Strikingly, no catalytic current enhancement was observed for **2** at the position of the Fe^{III}/Fe^{II} couple when examined in an oxygen-saturated acetonitrile solution in the presence of TFAH (10 mM) (Fig. 7A). As the Fe^{III}/Fe^{II} potentials of **2** and **1** are comparable, **2** was also expected to show electrocatalytic activity for the ORR. This unprecedented difference in reactivity implies that the ORR reactivity of these Fe complexes is not solely controlled by the Fe^{III}/Fe^{II} potential. Thus, at this point, we presume that the presence of a pseudo-macrocyclic ring in **1** might be a key factor in assisting electrocatalytic ORR. Next, we examined the electrocatalytic behavior of the Fe^{II} complex of the BPh_2L (**3a**). However, no catalytic current enhancement was observed at the position of the Fe^{III}/Fe^{II} couple of **3a** in the presence of O_2 and TFAH in acetonitrile at 25 °C (Fig. 7B). Likewise, no electrocatalytic ORR was observed for the Fe^{III} complex (**3**) in oxygenated acetonitrile in the presence of TFAH. Thus, the result implies that **3a** or **3** cannot promote electrocatalytic ORR. In **3a**, the introduction of the $-BPh_2$ group resulted in *ca.* 370 mV anodic shift of the Fe^{III}/Fe^{II} potential compared to **1a**, which could make the Fe^{II} electron-deficient and reduce the O_2 affinity of **3a** compared to **1a**. However, in the presence of TFAH, the position of the Fe^{III}/Fe^{II} potential of **3a** shifts to −0.25 V *vs.* Fc^+/Fc, similar to that of **1a** in the presence of TFAH.

Next, we correlated the experimental ORR data with the solid-state structures of the Fe^{II} complexes, which are summarized in Chart 2. In **2a**, the ligand core is considerably opened, and the distance between the two imine nitrogen atoms (3.056 Å) and oxime oxygen atoms (3.042 Å) is substantially elongated compared to the distances observed in **1a** ($d_{N(imine)-N(imine)}$ = 2.861 Å, $d_{O(oxime)-O(oxime)}$ = 2.492 Å). This is further indicated by the shortening of the N_{imine}–Fe–N_{imine} bond angle in **1a** (97.78°) compared to that in **2a** (103.87°). In contrast, the ligand cavity in **3a** is nearly similar to that of **1a**, as indicated by the closely similar N_{imine}–N_{imine} and O_{oxime}–O_{oxime} distances observed in **1a** and **3a**. If the presence of a macrocyclic ligand system is the only factor that enhances electrocatalytic ORR, then **3a** was also expected to exhibit ORR. Thus, these structural data indicate that the protonated oxime backbone has an important role in the electrocatalytic ORR. Additionally, we also experimentally observed the protonation of the ligand oxime scaffold in the presence of TFAH. These data together suggest that the oxime scaffold works as a proton exchanging site during the electrocatalytic ORR of **1**. If the position of the Fe^{III}/Fe^{II} potential is the only factor that controls the ORR, then we would have observed electrocatalytic ORR activity of the Fe complexes of three ligand systems presented here.

Chemical ORR study

We examined the ORR of the Fe^{III} complexes chemically in an O_2-saturated acetonitrile solution in the presence of excess amounts of Fc* and TFAH, and the reactions were monitored by UV-vis spectroscopy. Complex **1** is rapidly converted to **1a** in the presence of one equiv. of Fc* (Fig. S45†). The addition of catalytic amounts of **1** (0.02 mM) to an oxygen-saturated acetonitrile solution consisting of Fc* (1 mM) and TFAH (20 mM) resulted in an increase of absorbance maxima at 780 nm in the UV-vis spectrum (Fig. 8A), which corresponds to the formation of the decamethylferrocenium cation (Fc^{*+}). The formation of a large excess of Fc^{*+} suggests the occurrence of catalytic ORR. Investigation of the reaction solution by $Ti(O)SO_4$ assay revealed the absence of detectable H_2O_2 in the reaction solution (Fig. S46†), which implies that **1** works as a chemical ORR catalyst for the selective $4e^-/4H^+$ reduction of O_2 (eqn (4)).

$$O_2 + 4Fc^* + 4CF_3COOH \rightarrow 2H_2O + 4Fc^{*+} + 4CF_3COO^- \quad (4)$$

We further investigated the kinetics of the ORR by UV-vis spectroscopy. The concentration dependence of each reactant was evaluated by varying substrate concentrations under

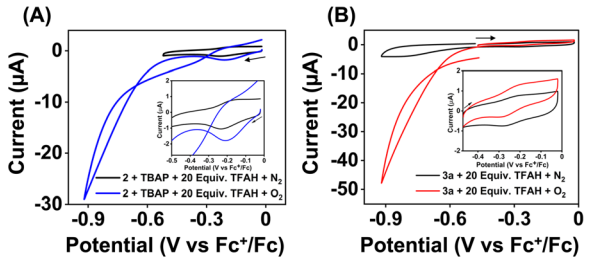

Fig. 7 Cyclic voltammograms of **2** (0.5 mM, (A)) and **3a** (0.5 mM, (B)) in the presence and absence of oxygen in acetonitrile containing 10 mM of TFAH and 50 mM $^nBu_4NPF_6$ as the supporting electrolyte at 25 °C. The inset data show a zoomed version of the Fe^{III}/Fe^{II} potential region. CV data were recorded using a 3 mm GC electrode at a 100 mV s^{-1} scan rate.

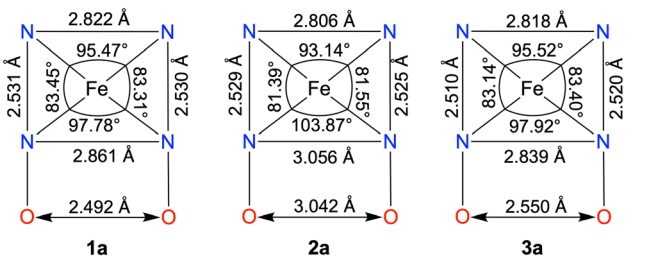

Chart 2 A comparison of the structural parameters of the Fe^{II} complexes.

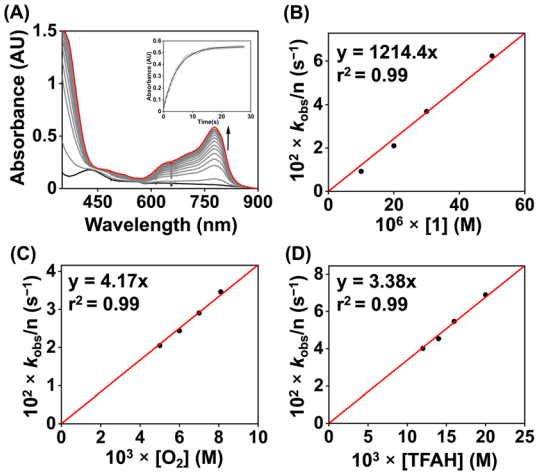

Fig. 8 (A) Change of the UV-vis spectrum of an oxygen-saturated acetonitrile solution containing 0.02 mM of **1**, 20 mM of TFAH, and 1 mM of Fc* at 25 °C. (B) A plot of k_{obs} *vs.* [**1**] at a fixed concentration of O_2 (8.1 mM), TFAH (20 mM) and Fc* (1 mM). (C) A plot of k_{obs} *vs.* [O_2] at a fixed concentration of **1** (0.02 mM), TFAH (20 mM), and Fc* (1 mM). (D) A plot of k_{obs} *vs.* [TFAH] at a fixed concentration of **1** (0.02 mM), Fc* (1 mM), and O_2 (8.1 mM).

pseudo-first-order reaction conditions and keeping the concentration of the other substrates constant (Fig. S47–S50†). The pseudo-first-order rate constant (k_{obs}) values were extracted from the slope of a plot of ln(ΔA) *vs.* time (s) at 780 nm (formation of Fc*$^+$). At a fixed concentration of TFAH (20 mM), Fc* (1 mM), and O_2 (8.1 mM), it was observed that the k_{obs} values increase with increasing concentration of the complex (**1**). A plot of k_{obs} *vs.* [**1**] follows a linear relationship (Fig. 8B), implying first-order dependence of the complex concentration towards the overall reaction rate. Likewise, we observed that a plot of k_{obs} *vs.* [O_2] and [TFAH] yielded a linear relationship, described in Fig. 8C and D, respectively. However, we noted that the k_{obs} values remained independent upon varying the concentration of Fc*, described in Fig. S51,† suggesting that the reaction rate of the ORR catalyzed by **1** is independent of the Fc* concentration. Thus, based on the kinetic investigations, we propose a rate equation for the chemical ORR catalyzed by **1**, described in eqn (5) and (6).

$$\text{Rate} = n_{cat}\text{d[Fc*}^+\text{]/d}t = k_{obs}[O_2]^1 \quad (5)$$

$$k_{obs} = k_{cat}[\text{complex}]^1[\text{TFAH}]^1 \quad (6)$$

where k_{cat} is the third-order catalytic rate constant of **1**. The rate expression suggests that the rate-determining step in the catalytic cycle should depend on the concentrations of **1**, acid, and O_2. A k_{cat} value of 6.07×10^4 M^{-2} s^{-1} has been estimated following eqn (6) and Fig. 8B. The k_{cat} value derived chemically is much smaller than the k_{cat} of the electrocatalytic ORR. It is important to note here that the observed rate equation for **1** is different from the reported ORR of a nonheme Fe complex of a non-macrocyclic N_3O donor ligand, where the reaction rate was found to depend on the concentrations of O_2, acid, and Fc*.[22] Likewise, the ORR catalyzed by another Fe complex of an N_3O donor set of ligands was reported to depend on a half-order of the complex concentration.[21] However, the rate equation described in eqn (5) and (6) is similar to the ORR catalyzed by substituted Fe porphyrins[45,52,53] and a Co–corrole complex.[54]

Furthermore, the catalytic ORR of **1** was performed in the presence of trifluoroacetic acid-*d* (TFAD), which exhibited a slowdown of the catalytic reaction and a kinetic isotope effect (KIE) of 1.3 (Fig. S52†). The chemically observed KIE value is close to the value obtained in the electrochemical measurements (Fig. S40†). The obtained KIE value suggests the involvement of a PCET reaction during the chemical ORR.

Additionally, to understand the ORR kinetics, we performed an Eyring analysis for **1** (Fig. 9). For that, we measured the k_{cat} value of the ORR at different temperatures (298–283 K). $\Delta H^{\ddagger}$ and $\Delta S^{\ddagger}$ values of 3.9 kcal mol^{-1} and −31.4 cal K^{-1} mol^{-1}, respectively, were obtained for **1**. From these values, a $\Delta G^{\ddagger}$ of 13.2 kcal mol^{-1} at 298 K was estimated. The observed $\Delta G^{\ddagger}$ value for **1** is close to the reported $\Delta G^{\ddagger}$ of the ORR of an Fe(N_3-$O_{carboxylate}$) (20.5 kcal mol^{-1} at 298 K),[21] Fe($N_3O_{phenolate}$) (10.1 kcal mol^{-1} at 298 K),[22] and Co(N_2O_2) complex (14 kcal mol^{-1} at 298 K).[55]

Next, we explored the chemical ORR of **2** (0.02 mM) in acetonitrile. In the presence of TFAH (20 mM), Fc* (1 mM), and **2** (0.02 mM) in an oxygen-saturated acetonitrile solution, a very slow formation of Fc*$^+$ was noted compared to the background reaction in the absence of **2** (Fig. S53†). The experiment implies that **2** doesn't enhance the chemical ORR effectively, which is also consistent with the inability of **2** to assist electrocatalytic ORR.

Then, we explored the chemical ORR study of **3** (0.02 mM) in acetonitrile in the presence of Fc* (1 mM) and TFAH (20 mM). Complex **3** was generated *in situ* by oxidizing **3a** using one equiv of ceric ammonium nitrate (CAN). Similar to **1**, **3** was also found to be a selective catalyst for $4e^-/4H^+$ reduction of O_2 chemically (Fig. S55†). A blank experiment in the absence of **3** showed very little formation of Fc*$^+$ (Fig. S56B†). A comparison of ORR studies revealed the requirement of a larger time for **3** than **1** (Fig. S57†) under identical reaction conditions. Kinetic studies in the presence of varying concentrations of different substrates were conducted, which revealed pseudo-zero-order kinetics behavior in the presence of different substrates (Fig. S58–S61†). The catalytic ORR was found to depend on the concentration of **3** and Fc*, and remained independent of the concentration of

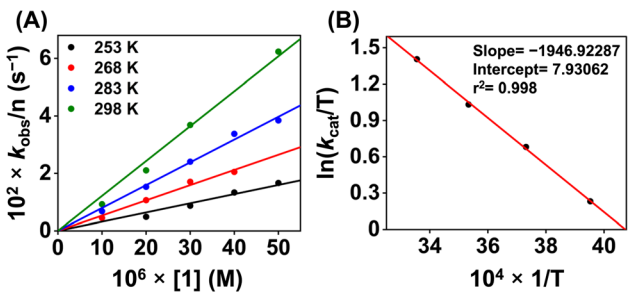

Fig. 9 (A) A plot of k_{obs} *vs.* [**1**] at different temperatures. (B) A plot of ln(k_{cat}/T) *vs.* 1/*T* for the estimation of activation parameters for **1**.

TFAH and O_2. The initial rate constant (k_i) for each of the substrate variation experiments was obtained from the slope of a plot of the [Fc*$^+$] (M) *vs.* time (s), and the observed k_i values were plotted against [substrate] to obtain the substrate dependence plot. The catalytic second-order rate constant (k_{cat}) was obtained using eqn (7) and Fig. 10A.

$$\text{Rate} = n_{cat}\text{d[Fc*}^+\text{]/d}t = k_{cat}[\text{complex}]^1[\text{Fc*}]^1 \quad (7)$$

A k_{cat} value of 2.47×10^2 M^{-1} s^{-1} was obtained at 25 °C for **3**. A TOF value of 2.4×10^{-1} s^{-1} has been calculated for **3** (Fig. S58D†). The ORR parameters of **1** and **3** have been described in Table 1.

Then we explored the Eyring analysis of **3** by measuring the k_{cat} of the ORR at different temperatures (Fig. 11). A $\Delta H^{\ddagger}$ and $\Delta S^{\ddagger}$ value of 8.7 kcal mol^{-1} and −31.5 cal K^{-1} mol^{-1}, respectively, were found for the ORR of **3**. Using these values, a $\Delta G^{\ddagger}$ of 18.7 kcal mol^{-1} has been estimated for **3**, which is significantly higher than that of **1**. Thus, the activation parameters suggest that the kinetic barrier for the ORR of **3** is higher than that for **1**.

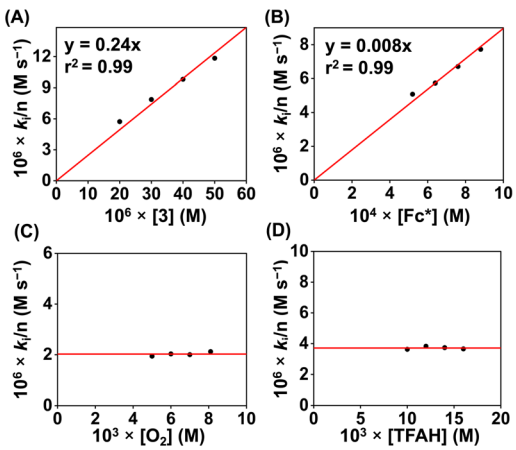

Fig. 10 (A) A plot of k_i *vs.* [**3**] at a fixed concentration of O_2 (8.1 mM), TFAH (20 mM), and Fc* (1 mM). (B) A plot of k_i *vs.* [Fc*] at a fixed concentration of **3** (0.02 mM), TFAH (20 mM), and O_2 (8.1 mM). (C) A plot of k_i *vs.* [O_2] at a fixed concentration of **3** (0.02 mM), TFAH (20 mM), and Fc* (1 mM). (D) A plot of k_{obs} *vs.* [TFAH] at a fixed concentration of **3** (0.02 mM), Fc* (1 mM), and O_2 (8.1 mM).

A comparison of the structural parameters of the Fe^{II} complexes (**1a** and **3a**) revealed that there are only slight differences in the metrical parameters between **1a** and **3a**. However, the chemical kinetics of the ORR of the Fe complexes are drastically different. Thus, the apparent reactivity difference can be attributed to the involvement of the oxime protons of the ligand in the PCET reactions for **1**. We suggest reversible protonation of the oxime backbone upon reduction of **1** in the presence of TFAH (*vide infra*). The protonated oxime-backbone is then involved in the intramolecular proton transfer reaction to the Fe–oxygen intermediate(s) formed in the ORR pathway for **1**. However, the borylated oxime arm in **2** is more electron deficient and doesn't participate in the reversible protonation reaction; rather, the CV measurement indicates the coordination of TFAH to the Fe center in the presence of an excess TFAH. We propose that this difference in the ligand architecture makes the rate-law of the ORR different for **1** and **3**. We recently described the $4e^-/4H^+$ reduction of O_2 by a molecular Co^{III} complex of HL, where the involvement of the protonated oxime arm of the ligand has been described.[41] The formation of a peroxo-bridged Co(III) dimer was evident at low temperatures in acetonitrile or acetone. However, no formation of such an intermediate was noted for the complex **1** in acetonitrile at low temperature. However, ORR selectivity and the reaction rate equation for both complexes are the same in acetonitrile. In addition, the k_{cat} values observed in the chemical ORR are also comparable for both Fe and Co complexes in acetonitrile.

Additionally, it has been shown that the catalytic ORR selectivity for $4e^-/4H^+$ reduction can follow a distinct 2 + 2 pathway for molecular Fe complexes.[21,22] To explore such a possibility, we initially investigated the reaction of **1** with one equiv. urea·H_2O_2, which showed a change in a single spectrum of **1** (Fig. S62A†). Furthermore, no significant change was encountered up to the addition of five equiv. of urea·H_2O_2. However, no decomposition of **1** also occurred, as evident from the UV-vis data. Next, we analyzed the reaction mixture after the addition of an excess of urea·H_2O_2 (5 equiv.) to **1** (incubated for 5 minutes) without any added proton and electron donor, which revealed unreacted H_2O_2 in the reaction solution (Fig. S62B†). If **1** simply catalyzes the disproportionation of H_2O_2 ($2H_2O_2 = 2H_2O + O_2$) *via* the formation of the $Fe^{n+}(O)$ intermediate,[56,57] the catalyst structure should be retained after the reaction.

Table 1 ORR parameters of the Fe complexes used in this study

Parameters	**1**	**3**
k_{cat}	6.07×10^4 M^{-2} s^{-1}, 2.7×10^7 M^{-2} s^{-1}[a]	2.5×10^2 M^{-1} s^{-1}
k_{obs} (s^{-1})	1.02×10^3[b]	2.4×10^{-1}
η (V)	0.98	—
$\Delta H^{\ddagger}$ (kcal mol^{-1})	3.9	8.7
$\Delta S^{\ddagger}$ (cal K^{-1} mol^{-1})	−31.4	−31.5
$\Delta G^{\ddagger}$ (kcal mol^{-1}), 298 K	13.2	18.1

[a] Determined by electrochemical measurements. [b] The value corresponds to TOF_{max}, measured at a scan rate of 6 V s^{-1} and TFAH concentration of 10 mM.

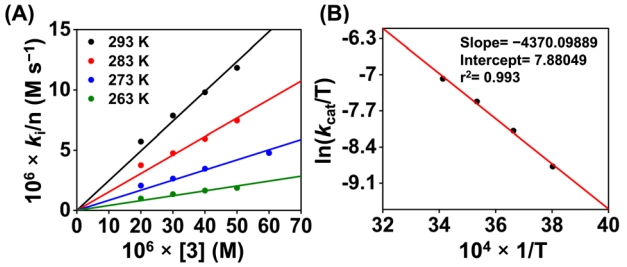

Fig. 11 A plot of k_i *vs.* [**3**] (A) at different temperatures. A plot of ln(k_{cat}/*T*) *vs.* 1/*T* for the estimation of activation parameters for **3** (B).

However, there is a clear change in the features of **1** in the presence of H_2O_2. Moreover, if the disproportionation reaction occurs in the mentioned time scale, the reaction is slower than the $4e^-/4H^+$ reduction of O_2 catalyzed by **1**. Thus, based on this experiment, we suggest that **1** undergoes a structural reorganization in the presence of added H_2O_2. However, this reactivity may not be relevant to the ORR mechanism of **1** (*vide infra*).

Next, we examined the reaction of **1** (0.02 mM) with urea·H_2O_2 (4 mM) in the presence of TFAH (20 mM), and Fc* (1 mM) under a nitrogen atmosphere and the reaction was monitored by UV-vis spectroscopy. The reaction also resulted in the $2e^-/2H^+$ reduction of H_2O_2 at 25 °C. The formation of Fc^{*+} is described in Fig. S63.† An induction-like behavior was observed initially in the time trace, which we suggest is because of the structural reorganization that occurred in the presence of H_2O_2. A pseudo-zero-order kinetics was observed in the presence of varying amounts of the substrates, described in Fig. S64–S71.† An initial rate of the formation of Fc^{*+} (k_i, M s^{-1}) was determined from a plot of [Fc^{*+}] *vs.* time (s) for different substrates. At a fixed concentration of TFAH and Fc*, the magnitude of k_i varies linearly with an increasing concentration of **1** (Fig. S65†). Likewise, k_i was found to be proportional to the concentration of urea·H_2O_2 (Fig. S67†). However, the k_i values remained independent of the concentration of TFAH and Fc* (Fig. S69 and S71†). Thus, the H_2O_2RR catalyzed by **1** follows eqn (8) and (9).

$$H_2O_2 + 2Fc^* + 2CF_3COOH \rightarrow 2H_2O + 2Fc^{*+} + 2CF_3COO^- \quad (8)$$

$$\text{Rate} = n_{cat}d[Fc^{*+}]/dt = k_{cat}[\text{complex}]^1[\text{urea}\cdot H_2O_2]^1 \quad (9)$$

Here k_{cat} is the second-order catalytic rate constant for the H_2O_2RR. A k_{cat} value of 1.2×10^2 M^{-1} s^{-1} was obtained for **1** at 25 °C using eqn (9) and Fig. S65.† Therefore, the kinetic studies described above discard the possibility of H_2O_2 being a reaction intermediate in the ORR pathway catalyzed by **1**. The observed ORR pathway of the Fe complexes (**1** and **3**) is different from the reported nonheme Fe catalysts, where the formation of H_2O_2 as an intermediate has been described.[19,22]

ORR mechanism

Based on the experimental observations, a possible reaction mechanism of the ORR of **1** is described in Scheme 2. $1e^-/1H^+$ reduction of the Fe^{III} complex (**1**) results in the formation of protonated Fe^{II} complex ($\mathbf{1a}^H$) following a PCET pathway. The ^{1}H NMR measurement of **1a** in the presence of an excess TFAH also supports the assignment. Then, the binding of O_2 to $\mathbf{1a}^H$ results in the formation of an $Fe^{III}(O_2^{\bullet})$ species (**1b**), which undergoes a PCET reaction to form an Fe^{III}(OOH) complex (**1c**). The species **1c** then undergoes a PCET reaction to form H_2O and the Fe^{III}–OH complex (**1d**).

Here, we propose that the protonated oxime backbone of the ligand is involved in the intramolecular proton transfer reaction to the distal OH group of the Fe–OOH moiety, possibly in the rate-determining step. **1d** then reacts with another equiv. of proton to yield another equiv. of H_2O and the starting Fe^{III} complex (**1**). For **3**, we speculate a reaction mechanism similar to that of **1**, except for the intramolecular PCET reaction as speculated in the case of **1**. Both chemical and electrochemical measurements established that the H_2O_2 formation *via* the $2e^-/2H^+$ pathway is not favored in the present study, compared to the reported 2 + 2 pathway of two nonheme Fe ORR catalysts.[21,22] We suggest that the protonated oxime backbone assists in the intramolecular proton transfer reaction to the distal oxygen atom of the Fe^{III}–OOH intermediate (**1c**) and helps in the O–O bond cleavage. Overall, the study highlights the importance of the presence of acidic protons in the vicinity of the redox-active center to assist the ORR. The effect of the secondary coordination sphere on ORR studies has been investigated for different Fe complexes of porphyrin and corrole-based ligand systems.[6–9] The presence of tertiary amine group(s) at the secondary coordination sphere increased the rate of the ORR by 2–3 times.[34] Likewise, the installation of carboxylic acid,[58,59] pendant primary amine and guanidine sites,[60] and phenanthroline backbone[61] at the secondary coordination sphere of Fe–porphyrin complexes was shown to enhance the ORR. The effect of proton relay sites installed in the Hangman carboxylic acid containing Co/Mn-porphyrin complexes[25,28] and Co–corrole complexes consisting of N^1,N^1-bis(pyridin-2-ylmethyl)ethane-1,2-diamine backbone at the secondary coordination sphere has been investigated.[33] Herein, we described the first example of

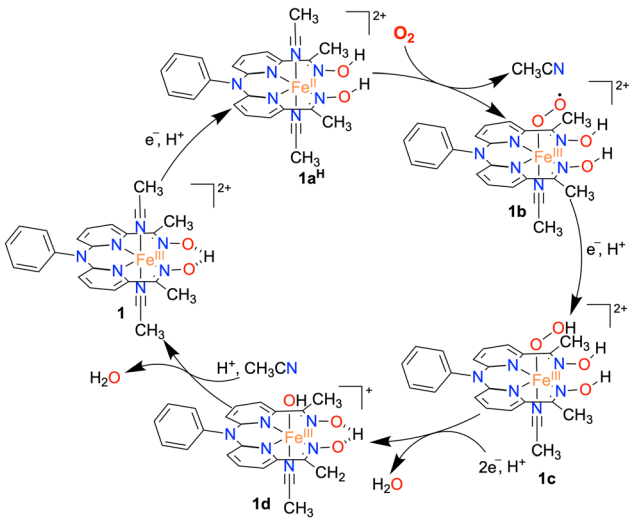

Scheme 2 The proposed mechanism of the ORR catalyzed by the Fe complex **1**.

a nonheme iron complex containing a proton relay site at the secondary coordination sphere that can catalyze the $4e^-/4H^+$ reduction of O_2.

Conclusions

n summary, we synthesized and thoroughly characterized the Fe complexes of N_4 donor ligands (H_2L, Me_2L, and BPh_2L). The X-ray structure of the Fe^{II} complexes has been determined, which revealed that similar structural parameters are present in **1a** and **3a**. However, **2a** exhibited different metrical parameters than **1a**/**3a**. The Fe^{III}/Fe^{II} reduction potential of **1a** and **2a** is much more cathodically shifted than **3a**, which suggests that Fe^{II} is more electron-rich in **1a**/**2a** than in **3a**. Electrocatalytic ORR of **1** has been investigated in acetonitrile, which revealed a selective $4e^-/4H^+$ reduction of O_2 to H_2O with a TOF_{max} of 1.02×10^3 s^{-1} and η_{eff} of 0.98 V. These parameters are often compared to access the catalytic efficiency of molecular complexes in the ORR. The TOF and η_{eff} of **1** compare well with the reported secondary coordination sphere edited Fe–porphyrin complexes utilized in the ORR study. Strikingly, **2** and **3** were found inactive towards the electrocatalytic reduction of O_2. Additionally, we examined the ORR of the Fe^{III} complexes chemically in the presence of a soluble reductant Fc*, which also revealed the occurrence of $4e^-/4H^+$ reduction of O_2 for **1** and **3**. Detailed kinetic studies of **1** were performed using spectrochemical studies. The catalytic rate equations for the chemical and electrochemical ORR of **1** are identical, demonstrating a similar reaction mechanism. However, complex **2** catalyzed chemical ORR in acetonitrile was very slow. Furthermore, **3** was found to follow different kinetics for the ORR, where the rate of the reaction depends upon the concentrations of the catalyst and reductant, inferring a different rate-limiting step during the chemical ORR of **3** than **1**. Furthermore, we noticed that the Fe^{II} complexes (**1a** and **3a**) have similar Fe–N bond distances and N–Fe–N bond angles. The only considerable difference between the Fe complexes (**1a** and **3a**) is the absence of oxime groups in **3a**. These experimental observations strongly suggest the importance of the oxime groups in assisting the ORR in the case of **1** and is the cause of following a different ORR mechanism from that of **3**. In fact, the presence of an intramolecular proton exchanging site in **1** causes a different rate-determining step for **1** than **3** for the chemical ORR. The inactivity of **2** towards the ORR is noteworthy. Despite having a similar $E_{1/2}$ of **1** and **2**, **2** doesn't enhance the ORR. The presence of the protonated oxime scaffolds in **1**, therefore, plays a crucial role in accelerating the ORR.

The effect of the proton relay source has been examined thoroughly in the case of Fe–porphyrin complexes by incorporating polar protic groups at the secondary coordination sphere of the porphyrin ring. To the best of our knowledge, such a proton relay factor in the ORR reaction of non-heme Fe complexes has not been described before. Thus, this study describes the first example of a nonheme Fe complex for ORR studies that contains a proton binding site at the secondary coordination sphere and accelerates the ORR through the intramolecular proton transfer reaction. The study highlights the ligand design aspects in developing non-heme ORR catalysts and showcases the secondary coordination sphere effect on the selective $4e^-/4H^+$ reduction of O_2. Our future efforts will focus on exploring the secondary coordination sphere effect on ORR studies using the nonheme ligands used in this study.

Data availability

All experimental data are available in the manuscript and ESI.†

Author contributions

AS and SP designed the project. AS has synthesized and characterized all ligands and Fe complexes described in this study. AS and AD performed the ORR studies. AS, AD, and SK analyzed the data. PJ and PPI assisted in the RRDE experiments. SP supervised the project. AS and SP wrote the original manuscript draft. All authors were involved in writing the manuscript.

Conflicts of interest

There are no conflicts to declare.

Acknowledgements

The research work is funded by the Science and Engineering Research Board (SERB, CRG/2022/005842). The authors gratefully acknowledge the Central Research Facility at IIT Delhi for the NMR and EPR measurements. X-ray crystal data of the iron complexes were measured in a DST-FIST-funded Bruker X-ray diffractometer (SR/FST/CSII-027/2014) at the Department of Chemistry, IIT Delhi. AS and AD thank the Indian Institute of Technology Delhi for a doctoral Fellowship.

Notes and references

1 S. Yoshikawa and A. Shimada, *Chem. Rev.*, 2015, **115**, 1936–1989.
2 M. Fernandez-Fernandez, M. A. Sanroman and D. Moldes, *Biotechnol. Adv.*, 2013, **31**, 1808–1825.
3 E. I. Solomon, D. E. Heppner, E. M. Johnston, J. W. Ginsbach, J. Cirera, M. Qayyum, M. T. Kieber-Emmons, C. H. Kjaergaard, R. G. Hadt and L. Tian, *Chem. Rev.*, 2014, **114**, 3659–3853.
4 H. A. Gasteiger and N. M. Markovic, *Science*, 2009, **324**, 48–49.
5 H. A. Gasteiger, S. S. Kocha, B. Sompalli and F. T. Wagner, *Appl. Catal., B*, 2005, **56**, 9–35.
6 S. Bhunia, A. Ghatak and A. Dey, *Chem. Rev.*, 2022, **122**, 12370–12426.
7 M. L. Pegis, C. F. Wise, D. J. Martin and J. M. Mayer, *Chem. Rev.*, 2018, **118**, 2340–2391.
8 W. Zhang, W. Lai and R. Cao, *Chem. Rev.*, 2017, **117**, 3717–3797.
9 S. Dey, B. Mondal, S. Chatterjee, A. Rana, S. Amanullah and A. Dey, *Nat. Rev. Chem*, 2017, **1**, 0098.
10 Y. Zhao, D. P. Adiyeri Saseendran, C. Huang, C. A. Triana, W. R. Marks, H. Chen, H. Zhao and G. R. Patzke, *Chem. Rev.*, 2023, **123**, 6257–6358.

11 C. W. Machan, *ACS Catal.*, 2020, **10**, 2640–2655.
12 A. Das, M. Bera, L. Mallick, B. Chakraborty and S. Paria, in *Oxygen Reduction Reaction*, ed. K. Sengupta, S. Chatterjee and K. Dutta, Elsevier, 2022, pp. 125–172, DOI: 10.1016/B978-0-323-88508-9.00014-8.
13 M. Costas, M. P. Mehn, M. P. Jensen and L. Que Jr, *Chem. Rev.*, 2004, **104**, 939–986.
14 S. Kal and L. Que, *JBIC, J. Biol. Inorg. Chem.*, 2017, **22**, 339–365.
15 M. Guo, T. Corona, K. Ray and W. Nam, *ACS Cent. Sci.*, 2019, **5**, 13–28.
16 W. Nam, *Acc. Chem. Res.*, 2015, **48**, 2415–2423.
17 K. Ray, F. F. Pfaff, B. Wang and W. Nam, *J. Am. Chem. Soc.*, 2014, **136**, 13942–13958.
18 H. S. Soo, A. C. Komor, A. T. Iavarone and C. J. Chang, *Inorg. Chem.*, 2009, **48**, 10024–10035.
19 L. Wang, M. Gennari, F. G. Cantu Reinhard, J. Gutierrez, A. Morozan, C. Philouze, S. Demeshko, V. Artero, F. Meyer, S. P. de Visser and C. Duboc, *J. Am. Chem. Soc.*, 2019, **141**, 8244–8253.
20 L. Wang, M. Gennari, F. G. Cantu Reinhard, S. K. Padamati, C. Philouze, D. Flot, S. Demeshko, W. R. Browne, F. Meyer, S. P. de Visser and C. Duboc, *Inorg. Chem.*, 2020, **59**, 3249–3259.
21 E. N. Cook, D. A. Dickie and C. W. Machan, *J. Am. Chem. Soc.*, 2021, **143**, 16411–16418.
22 E. N. Cook, S. L. Hooe, D. A. Dickie and C. W. Machan, *Inorg. Chem.*, 2022, **61**, 8387–8392.
23 X. Lu, Y.-M. Lee, M. Sankaralingam, S. Fukuzumi and W. Nam, *Inorg. Chem.*, 2020, **59**, 18010–18017.
24 R. B. Gennis, *Biochim. Biophys. Acta, Bioenerg.*, 1998, **1365**, 241–248.
25 R. McGuire Jr., D. K. Dogutan, T. S. Teets, J. Suntivich, Y. Shao-Horn and D. G. Nocera, *Chem. Sci.*, 2010, **1**, 411–414.
26 B. D. Matson, C. T. Carver, A. Von Ruden, J. Y. Yang, S. Raugei and J. M. Mayer, *Chem. Commun.*, 2012, **48**, 11100–11102.
27 S. Mukherjee, M. Mukherjee, A. Mukherjee, A. Bhagi-Damodaran, Y. Lu and A. Dey, *ACS Catal.*, 2018, **8**, 8915–8924.
28 G. Passard, D. K. Dogutan, M. Qiu, C. Costentin and D. G. Nocera, *ACS Catal.*, 2018, **8**, 8671–8679.
29 S. Bhunia, A. Rana, P. Roy, D. J. Martin, M. L. Pegis, B. Roy and A. Dey, *J. Am. Chem. Soc.*, 2018, **140**, 9444–9457.
30 A. Ghatak, S. Bhakta, S. Bhunia and A. Dey, *Chem. Sci.*, 2019, **10**, 9692–9698.
31 A. Singha, A. Mondal, A. Nayek, S. G. Dey and A. Dey, *J. Am. Chem. Soc.*, 2020, **142**, 21810–21828.
32 S. Mukherjee, A. Nayek, S. Bhunia, S. G. Dey and A. Dey, *Inorg. Chem.*, 2020, **59**, 14564–14576.
33 J. Han, N. Wang, X. Li, W. Zhang and R. Cao, *J. Phys. Chem. C*, 2021, **125**, 24805–24813.
34 S. Bhunia, A. Ghatak, A. Rana and A. Dey, *J. Am. Chem. Soc.*, 2023, **145**, 3812–3825.
35 R. Zhang and J. J. Warren, *J. Am. Chem. Soc.*, 2020, **142**, 13426–13434.
36 D. J. Martin and J. M. Mayer, *J. Am. Chem. Soc.*, 2021, **143**, 11423–11434.
37 A. W. Schaefer, M. T. Kieber-Emmons, S. M. Adam, K. D. Karlin and E. I. Solomon, *J. Am. Chem. Soc.*, 2017, **139**, 7958–7973.
38 R. L. Shook, S. M. Peterson, J. Greaves, C. Moore, A. L. Rheingold and A. S. Borovik, *J. Am. Chem. Soc.*, 2011, **133**, 5810–5817.
39 H. Kotani, T. Yagi, T. Ishizuka and T. Kojima, *Chem. Commun.*, 2015, **51**, 13385–13388.
40 A. W. Nichols, E. N. Cook, Y. J. Gan, P. R. Miedaner, J. M. Dressel, D. A. Dickie, H. S. Shafaat and C. W. Machan, *J. Am. Chem. Soc.*, 2021, **143**, 13065–13073.
41 A. Das, A. Ali, G. Gupta, A. Santra, P. Jain, P. P. Ingole, S. Paul and S. Paria, *ACS Catal.*, 2023, **13**, 5285–5297.
42 T. Owen, F. Grandjean, G. J. Long, K. V. Domasevitch and N. Gerasimchuk, *Inorg. Chem.*, 2008, **47**, 8704–8713.
43 A. Santra, G. Gupta, B. Biswas, A. Das, D. Ghosh and S. Paria, *Inorg. Chem.*, 2023, **62**, 9818–9826.
44 I. Vernik and D. V. Stynes, *Inorg. Chem.*, 1996, **35**, 6210–6220.
45 M. L. Pegis, B. A. McKeown, N. Kumar, K. Lang, D. J. Wasylenko, X. P. Zhang, S. Raugei and J. M. Mayer, *ACS Cent. Sci.*, 2016, **2**, 850–856.
46 P.-A. Jacques, V. Artero, J. Pecaut and M. Fontecave, *Proc. Natl. Acad. Sci. U. S. A.*, 2009, **106**, 20627–20632.
47 D. M. Harraz, S. Weng and Y. Surendranath, *ACS Catal.*, 2023, **13**, 1462–1469.
48 J. M. Saveant and E. Vianello, *Electrochim. Acta*, 1963, **8**, 905–923.
49 A. J. Bard and L. R. Faulkner, *Electrochemical Methods: fundamentals and applications*, John Wiley & Sons, Inc., New York, 2001.
50 E. S. Rountree, B. D. McCarthy, T. T. Eisenhart and J. L. Dempsey, *Inorg. Chem.*, 2014, **53**, 9983–10002.
51 R. Tyburski, T. Liu, S. D. Glover and L. Hammarstroem, *J. Am. Chem. Soc.*, 2021, **143**, 560–576.
52 D. J. Wasylenko, C. Rodriguez, M. L. Pegis and J. M. Mayer, *J. Am. Chem. Soc.*, 2014, **136**, 12544–12547.
53 M. L. Pegis, C. F. Wise, B. Koronkiewicz and J. M. Mayer, *J. Am. Chem. Soc.*, 2017, **139**, 11000–11003.
54 A. Rana, Y.-M. Lee, X. Li, R. Cao, S. Fukuzumi and W. Nam, *ACS Catal.*, 2021, **11**, 3073–3083.
55 Y.-H. Wang, Z. K. Goldsmith, P. E. Schneider, C. W. Anson, J. B. Gerken, S. Ghosh, S. Hammes-Schiffer and S. S. Stahl, *J. Am. Chem. Soc.*, 2018, **140**, 10890–10899.
56 A. Robert, B. Loock, M. Momenteau and B. Meunier, *Inorg. Chem.*, 1991, **30**, 706–711.
57 K. Sengupta, S. Chatterjee and A. Dey, *ACS Catal.*, 2016, **6**, 1382–1388.
58 C. T. Carver, B. D. Matson and J. M. Mayer, *J. Am. Chem. Soc.*, 2012, **134**, 5444–5447.
59 J. D. Soper, S. V. Kryatov, E. V. Rybak-Akimova and D. G. Nocera, *J. Am. Chem. Soc.*, 2007, **129**, 5069–5075.
60 A. Ghatak, S. Bhunia and A. Dey, *ACS Catal.*, 2020, **10**, 13136–13148.
61 A. Ghatak, S. Samanta, A. Nayek, S. Mukherjee, S. G. Dey and A. Dey, *Inorg. Chem.*, 2022, **61**, 12931–12947.